Proceedings of the 25th International Conference on
Port and Ocean Engineering under Arctic Conditions
June 9-13, 2019, Delft, The Netherlands

Identifying flexural-mode shapes of ice floes under wave actions using multivariate analysis

Hongtao Li[1], Ersegun Deniz Gedikli[1], Raed Lubbad[1]
[1] Department of Civil and Environmental Engineering, Norwegian University of Science and Technology, Trondheim, Norway

ABSTRACT

This paper analyzes experimental data collected during the HYDRALAB+ project: *Loads on Structure and Waves in Ice (LS-WICE)*. Several data analysis techniques, including Fast Fourier Transform, Upward Zero-Crossing, Genetic algorithm, and Dynamic Mode Decomposition (DMD) are applied. The results show that the wavelength under ice in the analyzed data does not deviate from the open water wavelength. More importantly, we show that ice floes bend with the same frequency as the incoming waves. In addition, we identify the dominant flexural-mode shapes and the associated nonlinearities. Multivariate analysis techniques, such as *Proper Orthogonal Decomposition* (POD) and *Smooth Orthogonal Decomposition* (SOD) methods are applied to the spatial and temporal responses of ice floes. The results show that modes based on the POD and SOD methods have similar spatial and temporal shapes. Applying both methods reveals that most of the motion energy is captured in a two-dimensional subspace of the phase space, where the sum of the first two modes correspond to more than 95% of the total system response. Lastly, the results of the multivariate analysis indicate that weak nonlinearity exists in the flexural motions of ice floes induced by waves.

KEY WORDS: Proper Orthogonal Decomposition; Smooth Orthogonal Decomposition; Ice floe; Flexural modes.

INTRODUCTION

In the recent decades, the Arctic region is attracting more attention, because of global climate change, technological progress, improved infrastructure, geopolitical shifting and increasing appetite for rich carbon-hydrogen resources in this area (Bennett, 2016). Driven by these factors, one of the growing research fields is wave-ice interaction.

Surface gravity waves and sea ice interact with each other in a complex manner and create a feedback system. Waves break up the ice (Kohout et al., 2014), contribute to ice melting (Squire, 2019), and push the ice around. Concomitantly, sea ice attenuates and scatters the waves (Bennetts et al., 2007, Collins III et al., 2015). There are many other physical processes involved such as vortex shedding (Rabault et al., 2019), overwash (Skene et al., 2015), ice bending (Meylan et al., 2015) and inelastic collisions of ice floes (Li and Lubbad, 2018). In the present study, we focus on wave induced bending of ice floes.

We investigate a dataset from the project: *Loads on Structure and Waves in Ice (LS-WICE)* (Tsarau, 2017). This project includes laboratory experiments that continued for three weeks, and were performed at Hamburg Ship Model Basin (HSVA) in 2016. The project goals were to study (1) wave attenuation/dispersion in different arrays of discrete ice floes (Cheng et al., 2017), (2) ice floe collisions induced by wave forcing (Li and Lubbad, 2018), (3) ice fracture due to wave actions (Herman et al., 2017), and (4) ice-structure interaction under wave conditions (Tsarau et al., 2017). In this paper, we apply a number of data analysis techniques, including Fast Fourier Transform (*fft*), Upward Zero-Crossing, Genetic algorithm, and multivariate analysis techniques, specifically, *Dynamic Mode Decomposition* (DMD), *Proper Orthogonal Decomposition* (POD) and *Smooth Orthogonal Decomposition* (SOD). Results from the Genetic algorithm show that wavelength under ice does not deviate from the open water wavelength. Results from the *fft*, the Upward Zero-Crossing, the Genetic algorithm and the DMD methods indicate that ice floes bend with the same frequency as the incoming wave frequency. The POD and SOD methods extract similar temporal and spatial modes where the first two modes capture more than 95% of the total response, and the successive two modes show weak nonlinearity.

EXPERIMENTAL SETUP

The experimental setup is shown in Figure 1 (a). The wave maker on the left extended through the width of the ice tank (10 m). Regular waves were generated and they propagated in the positive *x*-direction. On the right-hand side of the tank (around 70 m from the wave maker), parabolic beach was installed to dissipate the incoming waves. The ice cover consisted of 15 and 6 ice floes in the *x* and *y* directions, respectively; in addition to a large floe adjacent to the beach. The dimensions of the small ice floes were 3 m and 1.63 m along *x*- and *y*-direction, respectively. These floes were produced by cutting an intact ice using electrical saws. The ice cover spanned from 20 m to 69 m as shown in Figure 1 (a). The mean thickness of the ice was 31.1 mm. Young's modulus of the ice cover was measured as 41~77 MPa. The trim tank (see upper part of Figure 1 (b)) was an open water area for the generated waves to develop fully. In total, 12 reflective markers (see Figure 1 (a) and Figure 1 (c)) were placed on the upper surface of the ice. The 3-dimensional orthogonal translational positions of these markers were tracked by Qualisys cameras. In addition, wide-angle GoPro Silver camera was fixed on the sidewall to monitor the motions of the ice floes. In this paper, we investigate the responses of the ice floe that is highlighted by light magenta color, denoted as #A, in Figure 1 (a) and Figure 1 (c). We utilize the test run with the following wave parameters: wave frequency of 0.5 Hz and wave height of 25 mm.

DESCRIPTION OF THE ANALYSIS METHODS

Calculating wavelength through optimization

We obtain the phase difference needed for estimating the wavelength by using the genetic algorithm in MATLAB, i.e. the MATLAB function called *ga*. This algorithm solves an optimization problem, which is formulated as:

$$\varepsilon_j = \sqrt{\sum_{i=1}^{n} \left[z_{k,i} - A_{zk}^{(j)} \cos(2\pi f_k^{(j)} t_i + \varphi_k^{(j)}) \right]^2} \tag{1}$$

where $z_{k,i}$ is the i^{th} entry of vertical displacement measurement vector $\mathbf{z}_k \in \mathbb{R}^{n\times 1}$; k denotes the marker at k^{th} position ($k = 3, 4, \cdots, 8$ in this paper); j represents the j^{th} set of

parameters used in optimization; A_{zk}, f_k and φ_k are oscillation amplitude, frequency and phase of k^{th} marker.

$$\Delta\varphi_{k-2} = \varphi_{k+2} - \varphi_k \tag{2}$$

$$\Delta x_{k-2} = x^0_{k+2} - x^0_k \tag{3}$$

$$L_{k-2} = 2\pi \frac{\Delta x_{k-2}}{\Delta\varphi_{k-2}} \tag{4}$$

where $k = 3, 4, 5$ here to circumvent multiple modes at edges of ice floes (for brevity, see the arguments in Sakai and Hanai (2002) and Cheng et al. (2018)); and superscript $'0'$ indicates initial position of markers. Wavelength $\bar{L}$ is determined by taking the mean of L_{k-2}.

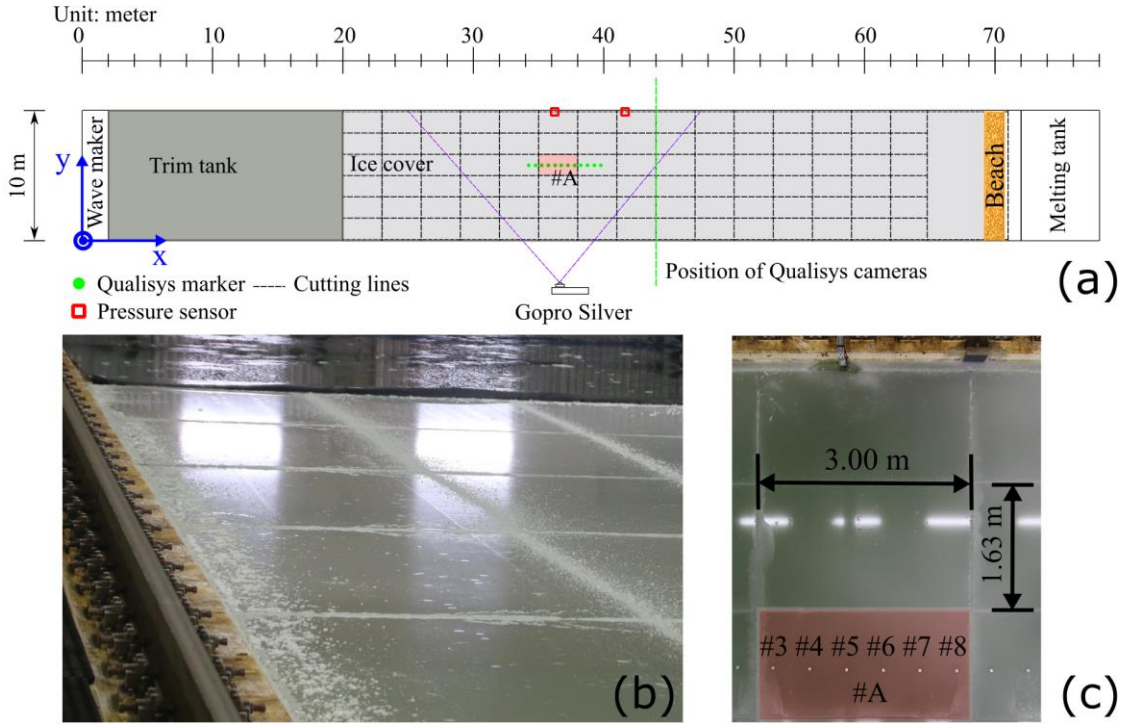

Figure 1. Experimental setup. (a) Schematic of experimental setup. (b) Image of trim tank (upper part) and ice cover (lower part). (c) Image showing the dimensions of individual ice floe and close view of ice floes instrumented with reflective markers. Light magenta color boxes in (a) and (c) highlight the ice floe #A that is of interest. Purple line in (a) illustrates the view area of GoPro Silver camera. Makers in (c) are numbered from #3 to #8 along the wave propagation direction.

Dynamic Mode Decomposition (DMD)

DMD is a way of decomposing time varying data (Taira et al., 2017, Schmid, 2010). In combination with the method of delay (Packard et al., 1980) with large time window, it resembles Fourier transform (Broomhead and King, 1986, Kutz et al., 2016). Amplitudes of dynamic modes and eigenvalues in the DMD method directly relate to power spectrum and frequency (Kutz et al., 2016). In this paper, we use the algorithm given in Tu et al. (2014) and Kutz et al. (2016).

Let $\mathbf{z}_k \in \mathbb{R}^{n\times 1}$ represent the measurement time history that has zero mean. The embedding dimension used here is $m = \lceil n/2 \rceil$, which gives a DMD spectrum that resembles the amplitude spectrum best.

Proper Orthogonal Decomposition (POD)

POD is also known as Singular Value Decomposition (SVD), Principal Component Analysis or Karhunen-Loève Expansion (Epps and Techet, 2010, Feeny and Kappagantu, 1998, Taira et al., 2017).

For synchronous measurements at r positions, measurement data matrix is $\mathbf{Z} = (\mathbf{z}_1, \mathbf{z}_2, \cdots, \mathbf{z}_r)$. In POD, we are looking for a orthonormal matrix $\mathbf{\Psi}$ that maximizes the variance of projections of $\mathbf{Z}$ on columns of $\mathbf{\Psi}$. This optimization problem can be solved by applying economical SVD as:

$$\mathbf{Z} = \mathbf{U}\mathbf{\Sigma}\mathbf{\Psi}^T \tag{5}$$

where columns of orthonormal matrix $U \in \mathbb{R}^{n\times r}$ represent temporal modes; square of diagonal singular value matrix $\mathbf{\Sigma} \in \mathbb{R}^{r\times r}$ gives proper orthogonal values (POVs) along diagonal, and columns of eigenvector matrix $\mathbf{\Psi} \in \mathbb{R}^{r\times r}$ are proper orthogonal modes (POMs).

Smooth Orthogonal Decomposition (SOD)

In SOD, we search for an orthonormal matrix $\mathbf{\Psi}$ to maximize the variance and smoothness of projections of $\mathbf{Z}$ onto columns of $\mathbf{\Psi}$ (Chelidze and Zhou, 2006). In this study, we apply the SOD method following Chelidze (2014) and Gedikli et al. (2018). For this optimization problem, we need the first time derivative matrix of $\mathbf{Z}$ in addition to data matrix $\mathbf{Z}$.

In SOD, Smooth Orthogonal Modes (SOMs) represent spatial mode shapes. Smooth Orthogonal Coordinates (SOCs) represent temporal mode shapes. Smooth Orthogonal Values (SOVs) represent the most dominant modes in the system based on their spatial distribution and smoothness of the SOCs.

Some important properties of SOD are: (I) columns of SOMs are linearly independent from each other; (II) columns of SOCs are orthogonal to each other but vector amplitude of each column is not one.

POD and SOD resemble each other where projections of $\mathbf{Z}$ onto POMs in POD are equivalent to SOCs in SOD. POMs are orthogonal to each other, and as mentioned above SOMs are linearly independent of each other. Therefore, POMs are comparable to orthogonalized SOMs when linear modes considered (Chelidze and Zhou, 2006).

PRE-PROCESSING OF THE DATA

Locating the steady-state time interval

We select a steady-state time interval from motion time histories of $\mathbf{z}_3$ and $\mathbf{z}_8$ as shown in Figure 2. This interval is chosen to satisfy two conditions, specifically, 1) it should ensure that there is no corruption from reflected waves, and 2) it should represent the best possible portion of the signal for steady-state. The detailed steps are as follows:

(1) Use the distances between the wave maker and the markers, and group velocity of waves at open water with intermediate water depths to determine the time of arrival (TOA) of waves at each marker.

(2) Calculate the traveling time (TT) of round-trip for waves from the location of each marker to the beach, by taking the ratio between the corresponding trip length and the group velocity.

(3) Add TT to TOA at each marker position to determine the last time instant (LTI) that is free from reflected waves for each marker.

(4) Select steady-state time interval between maximum of TOAs and minimum of LTIs.

Since marker #3 and marker #8 are to the left-most and right-most edges of the ice floe #A, steady-state time interval chosen using the above steps guarantees the steady-state condition and ensures that there is no effect from the reflected waves.

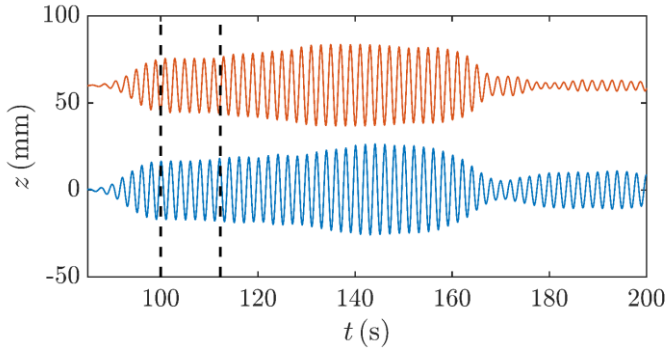

Figure 2. Identified steady-state time interval that is free from contamination of reflected waves (indicated by pair of black dashed lines). Light blue and orange lines represent marker #3 and #8, respectively. Data of marker #8 are shifted by 60 mm to aid visualization.

Distance between markers

The markers were placed with regular spacing of approximately 50 cm along the *x*-direction. To determine the longitudinal distance between these markers, we take the difference of the average *x*-position measurements of the markers before TOA.

RESULTS

Wavelength

Using the MATLAB function *ga*, viz., Eq. (1), we fit the measured vertical oscillations at each marker with a sinusoidal function. Figure 3 (a) shows such a fitting for marker #6 as an example. This process gives us the phases of oscillations for the different markers. By combining this information with the distance between these markers, and applying Eqs. (2)-(4), we find the estimate of the wavelength to be 6.16 m. This result is in agreement with wavelength in open water condition. For this test run, Cheng et al. (2018) confirmed that wavelength remains the same in the presence of ice cover as in open water. They reached this conclusion by using data from pressure sensors (see *Figure 5b* in Cheng et al. (2018)).

Vertical oscillations of markers

In addition to the MATLAB function *ga*, we apply another three methods, i.e., *fft*, DMD and Upward Zero-Crossing analysis to determine the oscillation amplitudes and frequencies of the

different markers on ice floe #A. As illustrated in Figure 3 (b), *ga*, DMD and Upward Zero-Crossing method yield similar estimates of the oscillation amplitudes. On the other hand, the *fft* method seems to underestimate the oscillation amplitudes. This can be attributed to the finite length of data (truncated by rectangular window), which limits the frequency resolution, resulting in a spread of the energy content (see the width of the base of the peak in Figure 3 (b)). This is a known caveat of *fft* and referred to as spectral leakage. In Figure 3 (d), it can be seen that markers oscillate with the same frequency as waves.

As shown in Figure 3 (c), the oscillation amplitude at each marker on floe #A is larger than 13 mm. However, the target wave amplitude in open water is 12.5 mm. In addition, we would expect to see wave attenuation when the waves are propagating under ice. This is based on full-scale observations as in Sutherland and Rabault (2016), Li et al. (2017), and Collins III et al. (2015). In an attempt to explain this inconsistency, we examined the measurements from the two nearby pressure sensors shown in Figure 1. Analysis results show that the wave amplitude at these two positions are 8.5 mm and 8.7 mm, respectively. These values are obtained after subtracting the hydrostatic water pressure and the effects from submergence on the dynamic water pressure. The reason of this apparent discrepancy between wave and ice-oscillation amplitudes is not investigated here any further and is highly recommended to be considered for future research.

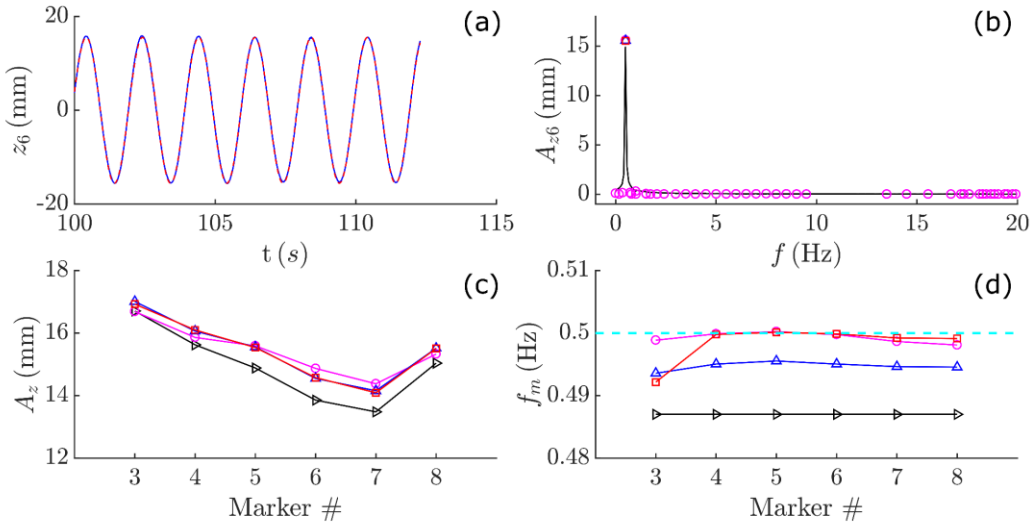

Figure 3. Oscillation amplitude and frequency of markers. (a) Vertical motion of marker #6 (blue line) and fitted motion (red dashed line) by Genetic algorithm. (b) Vertical oscillation amplitude and frequency of marker #6. Black line is amplitude spectrum obtained by *fft*. Magenta circles represent DMD spectrum. Blue triangle denotes result from Upward Zero-Crossing analysis. Red square denotes result from Genetic algorithm. (c) Oscillation amplitudes of markers #3 to #8. Red line with squares represents results from Genetic algorithm. Black line with right triangles denotes results from *fft.* Magenta line with circles indicates results from DMD. Blue line with triangles denotes results from Upward Zero-Crossing analysis. (d) Oscillation frequency of markers #3 to # 8; the same as in (c) plus that cyan line represents target frequency of generated waves.

Proper Orthogonal Value (POV) and Smooth Orthogonal Value (SOV)

We examine first the POVs and SOVs to determine the dominant modes in the interaction where they represent the energy in the system similar to Gedikli et al. (2017). As shown in Figure 4, the variation of the POVs and SOVs can be categorized into three distinct regions. Note that the SOV-based categorization results in more distinct identification (Figure 4 (b)).

From Figure 4 (a), it is seen that the sum of the first two modes account for 98.20% of the energy. Along with the successive two modes, the percentage rises to 99.70%. Figure 4 (b) reveals that the first two modes are similarly smooth. The same applies to mode pairs in the other two regimes.

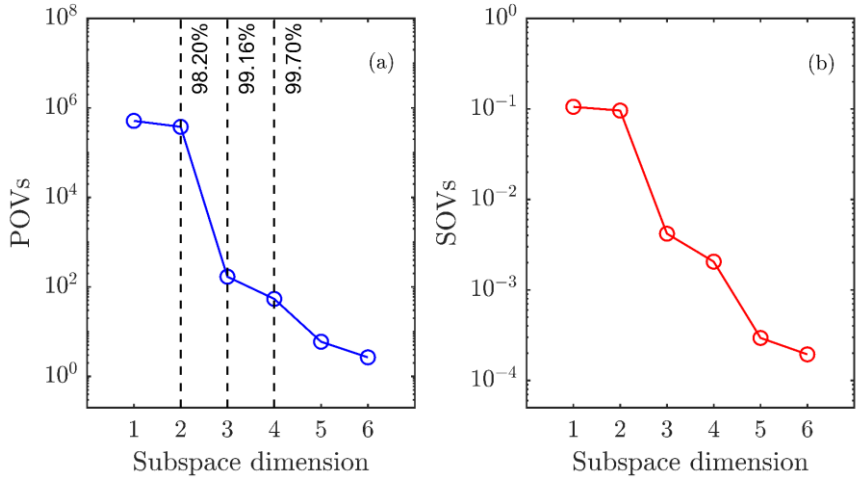

Figure 4. Proper orthogonal values (POVs) and smooth orthogonal values (SOVs). (a) POVs in the scale of logarithm with base 10. (b) SOVs in the scale of logarithm with base 10.

Temporal Modes (TMs) and Spatial Modes (SMs)

The POD and SOD methods result in similar TMs as illustrated in Figure 5. Figure 5 (a) and (b) show that the first two TMs appear to be sinusoidal. The first two TMs from SOD also resemble those from POD. Figure 5 (c) and (d) suggest that nonlinearity is embedded in the third and fourth modes. Modes in Figure 5 (e) and (f) represent the noise in the system, which accounts for less than 0.5% energy in the system (see Figure 4).

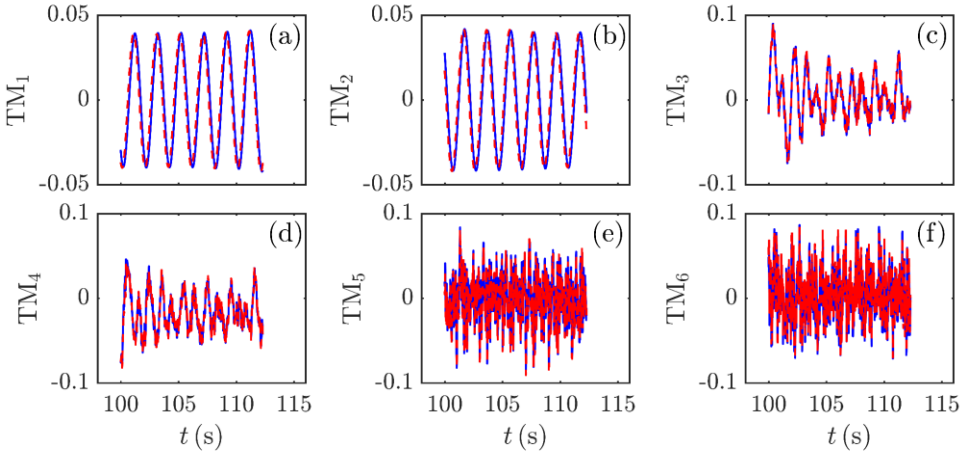

Figure 5. Temporal modes (TMs). Blue line denotes $\mathbf{U}$ from POD and red dashed line represents SOC from SOD. (a) First mode. (b) Second mode. (c) Third mode. (d) Fourth mode. (e) Fifth mode. (f) Sixth mode.

In Figure 6, we compare the SMs identified by the POD and SOD methods. These two methods give similar results. First two modes (Figure 6 (a) and (b)) look similar which resemble quarter of a sinusoidal shape. The third and fourth mode (Figure 6 (c) and (d)) resemble the first and second harmonic eigenmodes, respectively. Last two SMs (Figure 6 (e) and (f)) cannot be

simply justified as the third and fourth harmonic eigenmodes, because their energy content is minimal (see Figure 4), and also the limited length of ice floe does not allow these motions to fully develop.

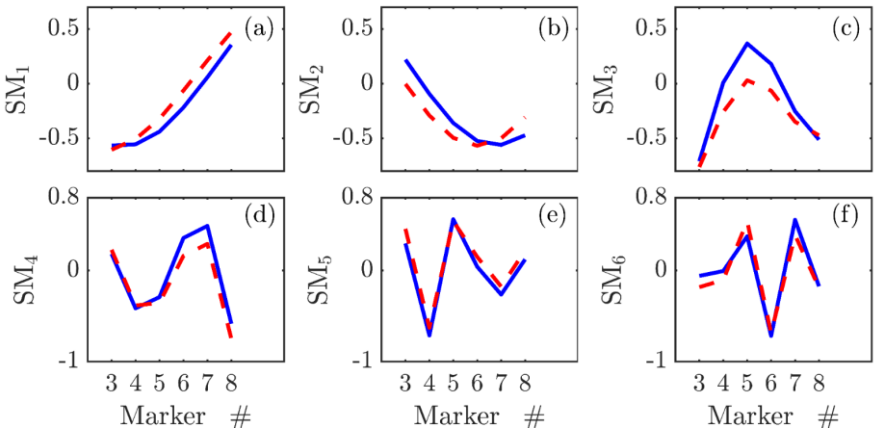

Figure 6. Spatial modes (SMs). Blue line denotes POM and red dashed line represents orthogonalized SOM. (a) First mode. (b) Second mode. (c) Third mode. (d) Fourth mode. (e) Fifth mode. (f) Sixth mode.

We perform spectral analysis on the TMs from the POD method to identify principal frequencies in each mode. Although we also find principal frequencies using SOD, we only illustrate the POD results for brevity.

Oscillation frequencies of first two modes match with the incident wave frequency as shown in Figure 7 (a) and (b). This suggests that combination of first two modes represents the dominant response due to the incident waves. The successive two modes have dominant frequency that are almost twice the wave forcing as shown in Figure 7 (c) and (d). These frequencies represent the collision frequencies that were identified in Li and Lubbad (2018) when considering collisions occur at both sides of the ice floe along *x*-direction. Figure 7 (e) and (f) show that the last two modes are contaminated by noise, which can also be seen in Figure 5. Results as shown in Figure 4, Figure 5 and Figure 7 suggest that first four modes are the most dominant modes, which account for more than 99 % of the total energy in the system's response; therefore, we hereafter only consider these four modes.

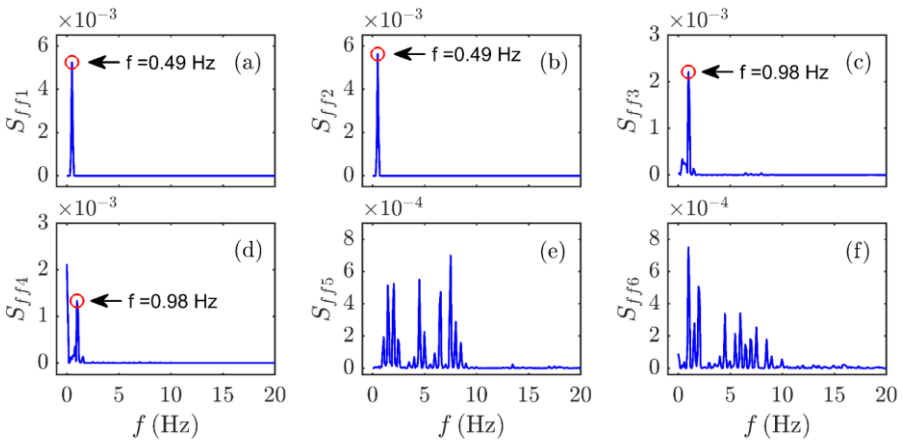

Figure 7. Spectral density of TMs using POD. (a) First mode. (b) Second mode. (c) Third mode. (d) Fourth mode. (e) Fifth mode. (f) Sixth mode.

We now apply a low-pass filter on the third and fourth TMs from the POD method. From Figure 7 (c) and (d), it is seen that no frequency content higher than 5 Hz has significant energy. Therefore, we select the cut-off frequency as 5 Hz.

Figure 8 illustrates the phase plane plots of the first four modes. It shows that first two modes form a limit cycle. Combinations of the second versus the third mode, and the second versus the fourth mode result in phase portraits that are similar to some combinations of crescent and figure eight type of responses. These results are more clear when the time evolution of these modes are investigated (not shown).

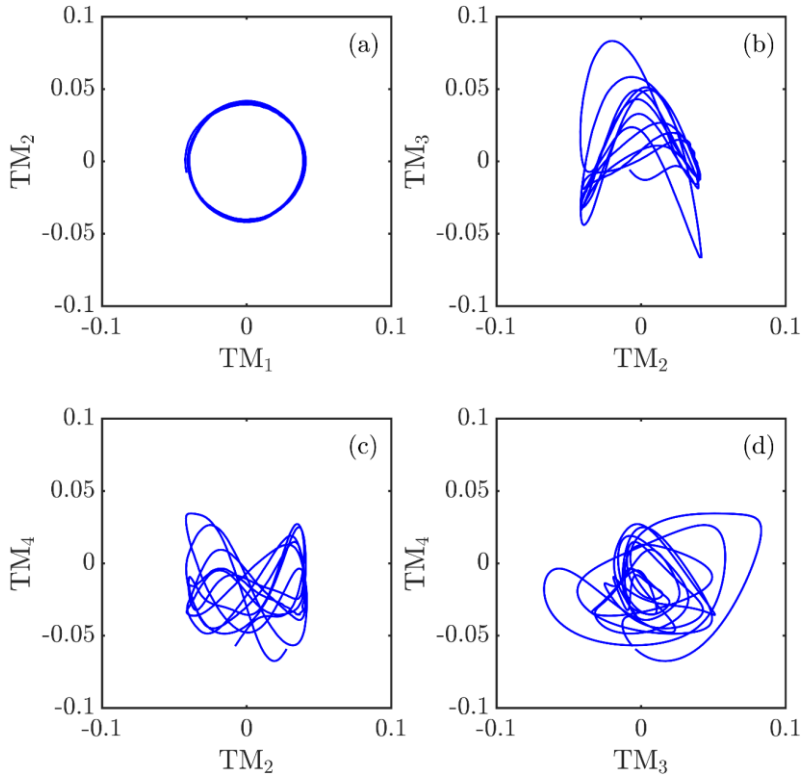

Figure 8. Phase plane plots of TMs from POD. (a) First mode versus second mode. (b) Second mode versus third mode. (c) Second mode versus fourth mode. (d) Third mode versus fourth mode.

Reconstruction using the POD and SOD methods

We now employ the first four modes obtained from the POD and SOD methods to reconstruct the response (i.e., the vertical oscillation of floe #A). Using normalized root mean error (NRMSE) as metric, we show that errors of reconstruction by POD and SOD are negligible as shown in Figure 9. Note that the root mean square error is normalized by standard deviation of the vertical displacement measurement to calculate NRMSE here. In general, POD and SOD produces similar reconstructed signals using the first four modes.

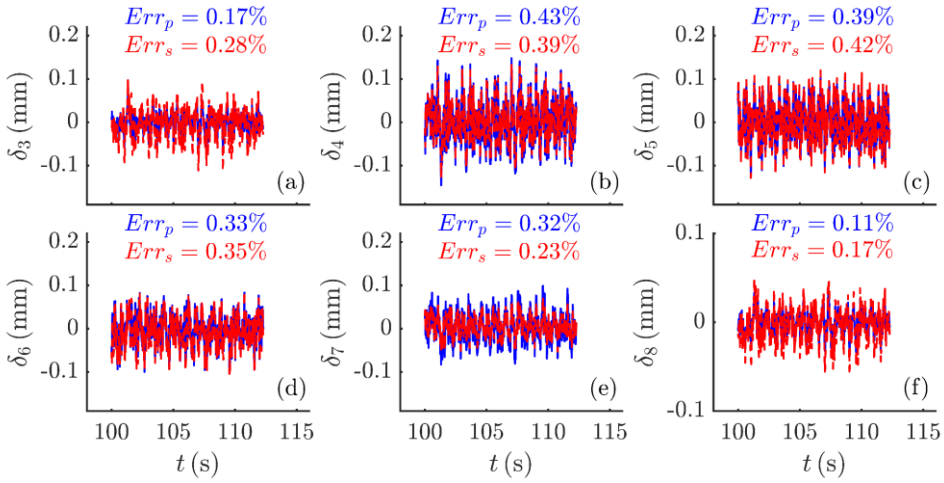

Figure 9. Reconstruction error for vertical displacement of each marker when using the first 4 modes of POD and SOD. (a) Marker #3. (b) Marker #4. (c) Marker #5. (d) Marker #6. (e) Marker #7. (f) Marker #8. Blue line shows results using POD and red dashed line represents results using SOD. Blue and red text denote NRMSE when using the first 4 modes of POD and SOD to reconstruct signals.

DISCUSSIONS

Rank of trajectory matrix $\mathbf{Z}$ in our case is not one, due to different oscillation phases of markers. Therefore, the SOD method is applicable for the measurements presented in this paper as in Chelidze and Zhou (2006). On the other hand, oscillation amplitudes of the markers (see Figure 3 (c)) are different and POVs are distinguishable (Figure 4 (a)). Therefore, POD is also suitable for analyzing data given in this paper (Chelidze and Zhou, 2006).

Figure 6 (a) and (b) show that the first two SMs resemble each other. In addition, corresponding first two TMs form a limit cycle on phase plane (see Figure 8 (a)). Thus, the first two dominant modes are actually one mode (Chatterjee, 2000). This is supported by Taira et al. (2017), who stated that traveling waves (in our case, waves propagating under ice cover) need two POD modes to be represented.

Because noise is high dimensional (Abarbanel et al., 1993), noise in generally is confined in the higher subspaces/modes in POD (Taira et al., 2017). Figure 5 (e) and (f) together with Figure 7 (e) and (f) illustrate the noise embedded in the system. Furthermore, corresponding SOVs that represent the most dominant modes are relatively small (see Figure 4 (b)) where these two modes are contaminated by noise.

CONCLUSIONS

In this paper, we characterize the response of ice floes in regular waves by analyzing data acquired during the LS-WICE project. By applying *fft*, Genetic algorithm, Upward Zero-Crossing analysis and DMD, we find that the ice floe of interest oscillates with a larger amplitude than waves, but with the same frequency as waves.

To identify the vibration modes of ice floes, we employ two multivariate analysis techniques, i.e., the POD and SOD methods. These two decomposition methods give similar temporal and spatial modes. Results from the POD and SOD methods suggest that the first two subspaces of the phase space (the first two modes that represent traveling wave) are dominant. The aggregated energy captured by these two modes are more than 95%. The third and fourth mode illustrate nonlinearity and oscillate at a frequency approximately twice of the incoming waves. When first four POD and SOD modes are used to reconstruct the signal, the resulting errors similar to each other and they are negligible.

As a result, we show that the POD and SOD methods are two effective methods to extract dynamic spatiotemporal characteristics for wave induced bending of ice floes. Here, we present the analysis of data from only one test run. In the near future, more comprehensive analysis results that include data from remaining test runs will be presented.

ACKNOWLEDGEMENTS

The authors wish to acknowledge the support from the Research Council of Norway through the Centre for Research-Based Innovation SAMCoT and the support from all SAMCoT partners. The experiment work described in this publication was supported by the European Community's Horizon 2020 Programme through the grant to the budget of the Integrated Infrastructure Initiative HYDRALAB+, Contract no. 654110. The lead author would like to thank the Hamburg Ship Model Basin (HSVA), especially the ice tank crew, for the hospitality, technical and scientific support and the professional execution of the test programme in the Research Infrastructure ARCTECLAB. The corresponding author would like to express gratitude towards colleagues in the LS-WICE project, including Prof. Hayley Shen and Meleta Truax from Clarkson University, Prof. Agnieszka Herman from University of Gdansk, Dr. Karl-Ulrich Evers from HSVA, Dr. Andrei Tsarau and Prof. Sveinung Løset form Norwegian University of Science and Technology and Dr. Sergiy Sukhorukov from Kvaerner AS.

REFERENCES

ABARBANEL, H. D., BROWN, R., SIDOROWICH, J. J. & TSIMRING, L. S. 1993. The analysis of observed chaotic data in physical systems. *Reviews of Modern Physics,* 65**,** 1331.

BENNETT, M. M. 2016. Discursive, material, vertical, and extensive dimensions of post-Cold War Arctic resource extraction. *Polar Geography,* 39**,** 258-273.

BENNETTS, L., BIGGS, N. & PORTER, D. 2007. A multi-mode approximation to wave scattering by ice sheets of varying thickness. *Journal of Fluid Mechanics,* 579**,** 413-443.

BROOMHEAD, D. S. & KING, G. P. 1986. Extracting qualitative dynamics from experimental data. *Physica D: Nonlinear Phenomena* 20**,** 217-236.

CHATTERJEE, A. 2000. An introduction to the proper orthogonal decomposition. *Current Science***,** 808-817.

CHELIDZE, D. 2014. Smooth local subspace projection for nonlinear noise reduction. *Chaos: An Interdisciplinary Journal of Nonlinear Science,* 24**,** 013121.

CHELIDZE, D. & ZHOU, W. 2006. Smooth orthogonal decomposition-based vibration mode identification. *Journal of Sound and Vibration,* 292**,** 461-473.

CHENG, S., TSARAU, A., EVERS, K. U. & SHEN, H. 2018. Floe size effect on gravity wave propagation through ice covers. *Journal of Geophysical Research: Oceans*.

CHENG, S., TSARAU, A., LI, H., HERMAN, A., EVERS, K.-U. & SHEN, H. 2017. Loads on Structure and Waves in Ice (LS-WICE) Project, Part 1: Wave attenuation and dispersion in broken ice fields. The 24th International Conference on Port and Ocean Engineering under Arctic Conditions, 2017 Busan, Korea.

COLLINS III, C. O., ROGERS, W. E., MARCHENKO, A. & BABANIN, A. V. 2015. In situ measurements of an energetic wave event in the Arctic marginal ice zone. *Geophysical Research Letters,* 42**,** 1863-1870.

EPPS, B. P. & TECHET, A. H. 2010. An error threshold criterion for singular value decomposition modes extracted from PIV data. *Experiments in Fluids,* 48**,** 355-367.

FEENY, B. & KAPPAGANTU, R. 1998. On the physical interpretation of proper orthogonal modes in vibrations. *Journal of Sound and Vibration,* 211**,** 607-616.

GEDIKLI, E. D., CHELIDZE, D. & DAHL, J. M. 2018. Bending dominated flexible cylinder experiments reveal insights into modal interactions for flexible body vortex-induced

vibrations. The 28th International Ocean and Polar Engineering Conference, 2018. International Society of Offshore and Polar Engineers.
GEDIKLI, E. D., DAHL, J. M. & CHELIDZE, D. 2017. Multivariate analysis of vortex-induced vibrations in a tensioned cylinder reveal nonlinear modal interactions. *Procedia engineering,* 199**,** 546-551.
HERMAN, A., TSARAU, A., EVERS, K.-U., LI, H. & SHEN, H. 2017. Loads on Structure and Waves in Ice (LS-WICE) Project, Part 2: Sea ice breaking by waves. The 24th International Conference on Port and Ocean Engineering under Arctic Conditions, 2017 Busan, Korea.
KOHOUT, A., WILLIAMS, M., DEAN, S. & MEYLAN, M. 2014. Storm-induced sea-ice breakup and the implications for ice extent. *Nature,* 509**,** 604.
KUTZ, J. N., BRUNTON, S. L., BRUNTON, B. W. & PROCTOR, J. L. 2016. *Dynamic Mode Decomposition: Data-driven Modeling of Complex Systems*, SIAM.
LI, H. & LUBBAD, R. 2018. Laboratory study of ice floes collisions under wave action. The 28th International Ocean and Polar Engineering Conference, 2018 Sapporo, Japan. International Society of Offshore and Polar Engineers.
LI, J., KOHOUT, A. L., DOBLE, M. J., WADHAMS, P., GUAN, C. & SHEN, H. H. 2017. Rollover of apparent wave attenuation in ice covered seas. *Journal of Geophysical Research: Oceans,* 122**,** 8557-8566.
MEYLAN, M., BENNETTS, L., CAVALIERE, C., ALBERELLO, A. & TOFFOLI, A. 2015. Experimental and theoretical models of wave-induced flexure of a sea ice floe. *Physics of Fluids,* 27**,** 041704.
PACKARD, N. H., CRUTCHFIELD, J. P., FARMER, J. D. & SHAW, R. S. 1980. Geometry from a time series. *Physical Review Letters* 45**,** 712.
RABAULT, J., SUTHERLAND, G., JENSEN, A., CHRISTENSEN, K. H. & MARCHENKO, A. 2019. Experiments on wave propagation in grease ice: combined wave gauges and particle image velocimetry measurements. *Journal of Fluid Mechanics,* 864**,** 876-898.
SAKAI, S. & HANAI, K. 2002. Empirical formula of dispersion relation of waves in sea ice. Ice in the environment: Proceedings of the 16th IAHR International Symposium on Ice, 2002. 327-335.
SCHMID, P. J. 2010. Dynamic mode decomposition of numerical and experimental data. *Journal of Fluid Mechanics,* 656**,** 5-28.
SKENE, D., BENNETTS, L., MEYLAN, M. & TOFFOLI, A. 2015. Modelling water wave overwash of a thin floating plate. *Journal of Fluid Mechanics,* 777.
SQUIRE, V. A. 2019. Ocean wave interactions with sea ice: a 2019 reappraisal. *Annual Review of Fluid Mechanics***,** 1-25.
SUTHERLAND, G. & RABAULT, J. 2016. Observations of wave dispersion and attenuation in landfast ice. *Journal of Geophysical Research: Oceans,* 121**,** 1984-1997.
TAIRA, K., BRUNTON, S. L., DAWSON, S. T., ROWLEY, C. W., COLONIUS, T., MCKEON, B. J., SCHMIDT, O. T., GORDEYEV, S., THEOFILIS, V. & UKEILEY, L. S. 2017. Modal analysis of fluid flows: An overview. *AIAA Journal***,** 4013-4041.
TSARAU, A. 2017. Data storage plan-Project HY+_HSVA-01 Experimental study on wave propagation in ice the the combined action of waves and ice on structures "Loads on Structures - Wave propagating in Ice" LS-WICE - Hamburg Ship Model Basin. LIMB: Hamburge Ship Model Basin.
TSARAU, A., SUKHORUKOV, S., HERMAN, A., EVERS, K.-U. & LØSET, S. 2017. Loads on Structure and Waves in Ice (LS-WICE) project, Part 3: Ice-structure interaction under wave conditions. The 24th International Conference on Port and Ocean Engineering under Arctic Conditions, 2017 Busan, Korea.
TU, J. H., ROWLEY, C. W., LUCHTENBURG, D. M., BRUNTON, S. L. & KUTZ, J. N. 2014. On dynamic mode decomposition: theory and applications. *Journal of Computational Dynamics,* 1**,** 391-421.